

# The effect of Al<sub>2</sub>O<sub>3</sub> fiber additive on braking performance of copper-based brake pads utilized in high-speed railway train

Peng Zhang<sup>a</sup>, Lin Zhang<sup>a,\*</sup>, Kangxi Fu<sup>a</sup>, Peifang Wu<sup>b</sup>, Jingwu Cao<sup>b</sup>, Cairang Shijia<sup>b</sup>, Xuanhui Qu<sup>a,\*\*</sup>

<sup>a</sup> Beijing Advanced Innovation Center for Materials Genome Engineering, Institute for Advanced Materials and Technology, University of Science and Technology Beijing, Beijing, 100083, China

<sup>b</sup> Beijing Tianyishangjia New Material Corp., Ltd., Beijing, 100094, China

## ARTICLE INFO

### Keywords:

Al<sub>2</sub>O<sub>3</sub> fiber additive  
Braking performance  
Tribo-film  
Copper-based brake pad

## ABSTRACT

Al<sub>2</sub>O<sub>3</sub> fiber was introduced into copper-based brake pads in order to improve the braking performance under high speed and heavy load. Two fabricated samples containing Al<sub>2</sub>O<sub>3</sub> fiber and no fiber additive were tested on a reduced-scale dynamometer using a special designed braking testing procedure. The results indicated Al<sub>2</sub>O<sub>3</sub> fiber additive mainly contributes to promote the increase of friction coefficient at relative low braking speeds and pressures and helps to stabilize the friction coefficient at high braking speed and heavy load. The addition of Al<sub>2</sub>O<sub>3</sub> fiber can also greatly reduce the wear loss of brake pads. Moreover, the sample with Al<sub>2</sub>O<sub>3</sub> fiber exhibits the lower maximum temperature during braking. Further, the relationship between braking properties and tribo-film is clearly revealed.

## 1. Introduction

High running speed and large carrying capacity is one of the goals of rail trains. In InnoTrans 2018, new high-speed railway concept trains have been proposed, which can achieve the free marshalling of 2–16 carriages and run at the maximum speed of 500 km/h [1]. This is a huge test for the train's braking system, because when the train experiences an emergency braking, it relies on the friction resistance, which is developed by the contact of copper-based brake pad and brake disc, to stop the train in a safe distance [2–4]. Generally, the copper-based brake pad applied in a high-speed railway train is composed of copper matrix, friction components and lubricants [5,6]. The much important characteristic during emergency braking is the dissipation of thermal energy through the brake pads and disc. Rodrigues et al. [7] specifically pointed out that copper softens at high temperature on the friction surface and thus acts as solid lubricant component, which is the main reason for the decline of the friction coefficient. Su et al. [8] also thought that the smooth and compacted exogenous copper third bodies play a solid lubrication role resulting in the reduction in friction coefficient under higher speed. Therefore, enhancing the strength of the copper matrix is one of the most important ways to maintain the elevated-temperature braking properties. In previous studies, ceramic

particles were most commonly used to enhance the braking performance of the copper-based brake pad. The addition of SiO<sub>2</sub>, ZrO<sub>2</sub> and Al<sub>2</sub>O<sub>3</sub> particles in composites can remarkably improve the friction and wear properties due to the reinforcement from those particles [6,9,10].

Except for granular ceramics, the fiber additive also facilitates the formation of contact plateaus and reduces the wear loss at higher temperature [11–14]. In the early study, Bijwe [11] found that fibers are responsible for enhancing the structural integrity of the friction composites due to their reinforcing nature. Inorganic fibers were reported to impart stable coefficient, excellent fade and wear resistance along with good mechanical strength [12–14]. For example, lapinus fiber can promote the fade resistance [12], and Satapathy et al. [13] also found that lapinus and basalt can improve the fade, recovery and wear characteristics. Al<sub>2</sub>O<sub>3</sub> fiber is a kind of the reinforcing component which has advantages of both ceramic particle and fiber. Kang et al. [15] revealed that under asymmetrical cyclic stressing, the part of the load shared by the matrix is gradually transferred to the Al<sub>2</sub>O<sub>3</sub> fiber with the increase of cyclic number, and the reinforcing role of the Al<sub>2</sub>O<sub>3</sub> fiber to the matrix is strengthened. Besides, the aligned short Al<sub>2</sub>O<sub>3</sub> fiber improves the resistance of the composite to ratchetting and stress relaxation under cyclic stressing and straining. Wang et al. [16] founded that hybrid metal matrix composites (MMC) with Al<sub>2</sub>O<sub>3</sub> fiber

\* Corresponding author.

\*\* Corresponding author.

E-mail addresses: [zhanglincs@163.com](mailto:zhanglincs@163.com) (L. Zhang), [quxh@ustb.edu.cn](mailto:quxh@ustb.edu.cn) (X. Qu).

<https://doi.org/10.1016/j.triboint.2019.03.034>

Received 22 December 2018; Received in revised form 12 March 2019; Accepted 13 March 2019

Available online 17 March 2019

0301-679X/ © 2019 Elsevier Ltd. All rights reserved.

and  $\text{Al}_2\text{O}_3$  particle shows the better wear resistance in comparison with the same amount of  $\text{Al}_2\text{O}_3$  particle reinforced MMC due to the 3-D distribution of fibers in hybrid-MMC which protects  $\text{Al}_2\text{O}_3$  particles from dropping-off. Moreover, Wang et al. [17] further pointed out that the wear resistance and the lubricant film of unhybrid-MMC with 20%  $\text{Al}_2\text{O}_3$  fiber are both better than that with hybrid  $\text{Al}_2\text{O}_3$  fiber and SiC particle.

As mentioned above, most of the results were drawn from the organic brake pad and the effect of  $\text{Al}_2\text{O}_3$  fiber on braking performance of copper-based brake pads has never been reported. This work introduced  $\text{Al}_2\text{O}_3$  fiber into copper-based brake pads in order to achieve better braking performance, and the main concern was on the variation of friction coefficient, wear loss, temperature and tribo-film caused by the addition of  $\text{Al}_2\text{O}_3$  fiber. Moreover, a reduced-scale braking tester was used with a special designed experimental procedure, which comes from the simplification of the technical condition for the brake pads applied in high-speed railways trains (TJ/CL 307-2014) [18]. Those works are effective to promote the design, preparation and testing of high-performance copper-based brake pad.

## 2. Experimental

### 2.1. Materials

The samples used in this paper are composed of substrate composition and  $\text{Al}_2\text{O}_3$  fiber additive, as shown in Table 1. The substrate composition is the mixture which mainly consists of matrix (electrolytic Cu, 99.5% purity, 48–75  $\mu\text{m}$ ), friction components (high-carbon CrFe, 95% purity, < 74  $\mu\text{m}$ ; water-atomised Fe, 99% purity, < 74  $\mu\text{m}$ ) and lubricant (graphite powder, 95% purity, 270–400  $\mu\text{m}$ ;  $\text{MoS}_2$  powder, 99% purity, < 18  $\mu\text{m}$ ). All commercial powders are supplied by Beijing Xing Rong Yuan Technology Co., Ltd. When  $\text{Al}_2\text{O}_3$  fiber additive was added, the content of copper powder was reduced accordingly. All percentages are weight percentage. Because excessive fiber additive in the matrix can aggravate the aggregation of fiber and seriously divide the matrix, we only added 3%  $\text{Al}_2\text{O}_3$  fiber additive to the copper-based brake pads (AF). The morphology of  $\text{Al}_2\text{O}_3$  fiber is shown in Fig. 1(a).  $\text{Al}_2\text{O}_3$  fibers are between 5 and 10  $\mu\text{m}$  in diameter and between 50 and 100  $\mu\text{m}$  in length. Besides, in order to reveal the effect of adding  $\text{Al}_2\text{O}_3$  fiber, the sample without  $\text{Al}_2\text{O}_3$  fiber (OF, the ingredients are shown in Table 1) was prepared. The preparation process was consistent with that of AF. The powders were blended in a V-shaped mixer for 8 h and cold-pressed at 400 MPa in steel die, then sintered with the steel backing at 950  $^\circ\text{C}$  for 2 h in  $\text{H}_2$  atmosphere under a pressure of 3 MPa.

### 2.2. Experimental methods

The braking tests were conducted on a reduced-scale braking tester (TM-1, Xi'an Shuntong Institute of Mechanical and Electrical Applied Technology, China). The special morphologies and functions have been reported in the literature [19]. Fig. 1(b) shows the fabricated samples. The friction area of the sample is 1560  $\text{mm}^2$ . The four samples were mounted on two fixtures (Fig. 1(c)), respectively, and then installed symmetrically on the both sides of the brake disc (Fig. 1(d)). The mating material was alloy steel (30CrSiMoVA), and the chemical composition is shown in Table 2. The hardness of the disc was in the range of 38–44 HRC. The diameter of brake disc is 400 mm and the thickness of brake disc is 20 mm. The average friction radius is 155 mm.

**Table 1**

Compositions of copper-based brake pads (wt. %).

	Copper	CrFe	MoS2	Fe	Graphite	Additive	Others
AF	53	8	2	18	10	3% $\text{Al}_2\text{O}_3$ fiber	6
OF	56	8	2	18	10	–	6

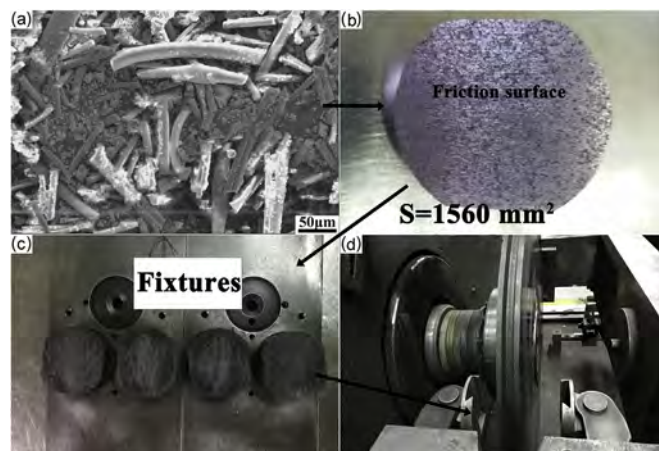


**Fig. 1.** (a) Image of  $\text{Al}_2\text{O}_3$  fiber, (b) fabricated samples, (c) testing samples and (d) pad-on-disk configuration.

Before performing the braking test, the surfaces of the brake pad and mating material were polished with 400-grit and 800-grit sandpaper. A micrometer was used to measure different positions of the brake pad and the mating disc separately to ensure that the two surfaces were smooth enough to produce a good fit. A thermocouple was located in the hole about 6 mm beneath the contact surface of brake pad. The experiment started with a moment of inertia of 44  $\text{kg}\cdot\text{m}^2$  corresponding to 5.7 tons of mass to be stopped per disk in the real train. The inertia was calculated in proportion from the inertia of the actual train. The proportion is related to friction area and radius in the experiment and that in the actual train.

Moreover, the braking experiments were conducted through four different stages (I - IV) in turn, as shown in Fig. 2. The first stage (I) was carried out at low pressure and braking speeds, and pressure increases from stage I to III. Under each braking pressure, the braking speed increases from low to high. The fourth stage (IV) was designed to verify the braking performance of brake pads after experiencing a series of emergency braking (generally speaking, the braking speed and pressure of high-speed railway train in the case of non-emergency braking is the condition presented by fourth stage). After each experiment, when the temperature exceeds the temperature set by the experiment program, the experiment would not start and the air-cooling system would be turned on automatically until the temperature measured by the thermocouple is lower than the temperature set by the program. This ensures that the starting temperature of each experiment is consistent. In this experiment, the room temperature was 25  $^\circ\text{C}$  and the program set a starting temperature of 60  $^\circ\text{C}$ . Thus, except that the first experiment started at 25  $^\circ\text{C}$ , all the other experiments started when the air-cooling system made the temperature detected by thermocouple lower than 60  $^\circ\text{C}$ . After the whole test, the wear loss was tested by an analytical balance with an accuracy of 0.01 g. According to the manufacturer's instructions, the relevant errors in the experiment are as follows: The error of test speed is  $\pm 10$  r/min; The error of test pressure is  $\pm 1\%$ ; The error of moment of inertia is lower than 0.001  $\text{kg}\cdot\text{m}^2$ ; The error of test temperature is  $\pm 2$   $^\circ\text{C}$ ; The relative error of test accuracy is  $\pm 1\%$ ; The error of test repeatability is  $\pm 1\%$ .

### 2.3. Characterization

Density was measured via Archimedes' principle. The Brinell hardness of the brake pad was tested on the HB-3000 hardness tester under a load of 250 kgf and time of 15 s. The shear tests were conducted on mechanical testing machine (ESIDA-L-2000) in order to measure the bending behavior of composites in the friction directions. The morphology of the powders and microstructure of the tested friction materials were observed on a scanning electron microscopy (SEM, JSM-

**Table 2**  
Chemical composition of 30CrSiMoVA (wt. %).

Element	C	Si	Mn	P	S	Cr	Mo	V	Fe
wt. %	0.27–0.33	0.45–0.65	0.55–0.75	≤0.025	≤0.025	1.00–1.50	0.40–0.60	0.20–0.30	Balance

Pressure (MPa)	Rotation speed (r/min)	Braking speed (km/h)
0.21 <b>I</b>	1110	120
	1480	160
	1845	200
	2025	220
0.41 <b>II</b>	465	50
	745	80
	1110	120
	1480	160
	1845	200
	2025	220
	2300	250
	2770	300
	2945	320
	3220	350
0.57 <b>III</b>	1110	120
	1480	160
	1845	200
	2025	220
	2300	250
	2770	300
	2945	320
	3220	350
	3500	380
	0.41 <b>IV</b>	1110
1110		120
1110		120

Fig. 2. The special designed experimental procedures on TM-1.

6510A) equipped with energy dispersive X-ray spectroscopy (EDS). The 3D morphology and roughness analysis were performed on a Laser Scanning Microscope (OLS4500).

### 3. Results and discussion

#### 3.1. Microstructure and physical properties

Fig. 3 exhibits the backscattered electron (BSE) images of sintered samples. Fig. 3(a) shows obvious existence of Al<sub>2</sub>O<sub>3</sub> fibers in the sample. The microstructure of OF in Fig. 3(b) is similar to that of AF except for the existence of Al<sub>2</sub>O<sub>3</sub> fibers. Table 3 shows the partial properties of brake pads. AF shows higher porosity. When adding the Al<sub>2</sub>O<sub>3</sub> fiber in copper-based brake pad, they can create more interface and cause the discontinuous matrix structure. The orders of Brinell hardness and shear strength are as follow:

Brinell hardness: AF < OF; Shear strength: AF < OF.

OF exhibits the higher Brinell hardness and shear strength due to the lower porosity. Interestingly, although the fiber is effective to improve the mechanical properties [20], the porosity seems to be the decisive

factor for Brinell hardness and shear strength that lower porosity can induce higher mechanical strength. However, the mechanical properties of AF are not actually lower. From the literature [19], the porosity, Brinell hardness and shear strength of commercial copper-based brake pads are 21.1%, 13.5 HB and 11 MPa, respectively. Besides, for the copper-based brake pads used in high-speed railway train fabricated by Xiao et al. [6], the density, Brinell hardness and shear strength of commercial copper-based brake pads are 4.8 g/cm<sup>3</sup>, 15 HB and 16 MPa, respectively. The porosity of AF is slightly lower, also the shear strength and Brinell strength of AF are both higher than that of reported brake pad [6,19]. From the technical condition of TJ/CL 307–2014 [18], the required Brinell hardness should be within the range of 10–30 HB and the shear strength should be greater than 6 MPa. The mechanical properties of AF meet those conditions very well.

#### 3.2. Friction and wear behavior

In order to reveal the effects of braking speed and pressure on brake performance, instantaneous friction coefficient ( $\mu_i$ ) and temperature ( $T_i$ ) of AF at different braking speeds and pressures are shown in Figs. 4 and 5. Fig. 4 shows the effects of braking pressure at different braking speeds. When the braking speed is 200 km/h, Fig. 4(a), during the first 20s of braking,  $\mu_i$  is similar with each other at three different pressures, then the  $\mu_i$  is lower at higher braking pressure. The higher braking pressure also results in the shorter braking time. The decreased  $\mu_i$  at higher applied pressure was also observed by Gultekin [21] and Uyyuru [22]. This originates from the flatter friction surface at higher braking pressure. However, during the last period of braking, the  $\mu_i$  increases sharply, which was commonly called anti-fade. The variation of  $T_i$  at different pressure is shown in Fig. 4(b). At the braking pressure of 0.21 MPa, 0.41 MPa and 0.57 MPa, the maximum  $T_i$  is about 120 °C, 125 °C and 130 °C, respectively. The influence of braking pressure on the maximum  $T_i$  is limited, while the increasing rate of  $T_i$  increases obviously with increase of pressure by comparing the slope of the  $T_i$ -time curve. Further, the influence rule of pressure on  $\mu_i$  and  $T_i$  is similar at 200 km/h, 300 km/h and 380 km/h, respectively. Compared with Fig. 4(a),(c) and (e), as the braking pressure increases, the braking duration is shorter and the friction coefficient is lower. Compared with Fig. 4(b),(d) and (f), the maximum  $T_i$  is slightly higher at the same braking speed and higher braking pressures, and the increasing rate of  $T_i$  dramatically increases with the increase of brake pressure.

Fig. 5 aims to reveal the effect of braking speed at different braking pressures. At the lowest pressure (0.21 MPa) in Fig. 5(a), the  $\mu_i$  is low in the initial stage at the braking speed of 120 km/h. In the initial stage of braking, there is more graphite exposed to the friction surface, which can provide better lubrication. As the braking continuous, the  $\mu_i$  increases gradually to the maximum as the rotational speed of brake disc decreases. When the friction surface is covered by a tribo-film, the lubrication is weaker than graphite. The lower rotational speed means lower shear strength, inducing higher friction resistance from the asperities, which is also the reason why the  $\mu_i$  continuous to rise. As the braking speed increases to 200 km/h, the fluctuation of  $\mu_i$  is similar to that at 120 km/h except for the longer braking time and slightly higher  $\mu_i$ . However,  $\mu_i$  is the lowest when the braking speed reaches to 220 km/h. In Fig. 5(b), the sample tested at higher braking speed shows significantly higher maximum  $T_i$  and the increasing rate of  $T_i$  also increases with the increase of braking speed. When the pressure is 0.41 MPa in Fig. 5(c), the fluctuation of  $\mu_i$  at 120 km/h and 200 km/h is similar to that at 0.21 MPa in Fig. 5(a). When the braking speed is

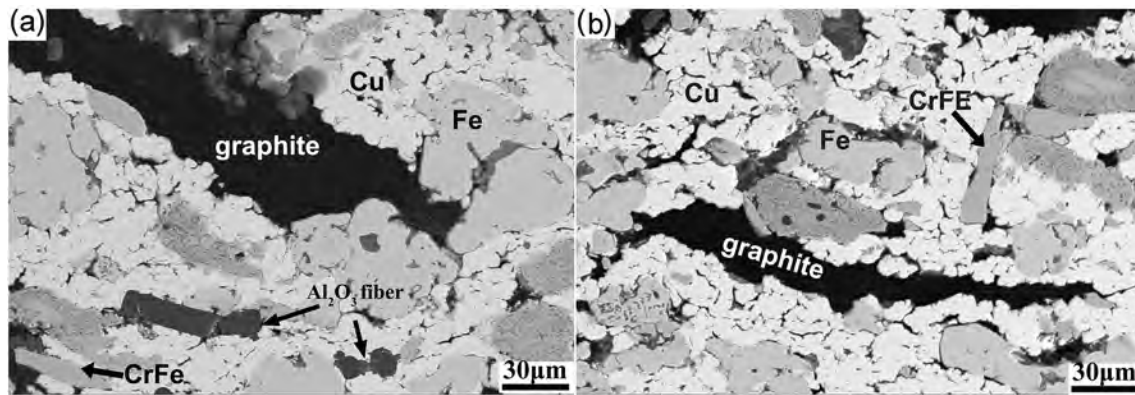


Fig. 3. BSE images of AF (a) and OF (b).

Table 3  
Partial properties of brake pads.

Samples	Density ( $\text{g}/\text{cm}^3$ )	Porosity (%)	Hardness (HB)	Shear strength (MPa)
AF	$5.00 \pm 0.07$	$19.5 \pm 1.1$	$22.7 \pm 2.1$	$37.18 \pm 1.2$
OF	$5.26 \pm 0.09$	$16.9 \pm 1.4$	$27.3 \pm 1.7$	$47.81 \pm 1.1$

300 km/h and 380 km/h, a platform stage appears in the  $\mu_i$  - braking time curve after experiencing a gradual increase. Contrast to that at the lower braking speed, the higher braking speed can cause more serious damage to the friction surface and make the friction surface flatter, which induces the reduction of friction resistance. Thus, as the rotational speed of the brake disc decreases, the friction resistance increases to a maximum, inducing the stable  $\mu_i$  at the platform stage until the end of the braking. At higher braking speed, the enhanced oxidation on friction surface also contributes to the appearance of platform stage of  $\mu_i$ . The  $\mu_i$  increases as the braking speed increases from 120 km/h to 300 km/h and then decreases when the braking speed is 380 km/h. The slightly lower  $\mu_i$  at 380 km/h than that at 300 km/h also indicates a more rapid material flow on the friction surface. Fig. 5(d) shows that higher braking speed means more transformation of thermal energy. Hence, the brake pads show the higher temperature. The influence rules of braking speed on  $\mu_i$  and  $T_i$  at 0.57 MPa in Fig. 5(e) and (f) are similar with that at 0.41 MPa. Summarizing Figs. 4 and 5, we can get the following conclusions:

- For the factor of pressure,  $\mu_i$  decreases as the braking pressure increases. According to the friction binomial theorem [31],  $\mu_i$  is proportional to the real contact area. Although the higher pressure can induce the higher  $\mu_i$  because of larger contact area, the flatter friction surface plays the leading role to reduce the  $\mu_i$ . During the whole braking process, the increased pressure not only slightly increases the maximum  $T_i$  pressure, but also significantly accelerates the increasing rate of  $T_i$ . This is consistent with the previous description that the temperature is also high at high loads during pin on disc test [19,29]. However, the difference in maximum  $T_i$  in Fig. 4(b),(d) and (f) is about 10 °C, 20 °C and 10 °C, respectively. This means that increase of maximum  $T_i$  caused by higher pressure is limited.
- For the factor of braking speed, in a certain range of braking speed,  $\mu_i$  increases with the increase of braking speed, and when it exceeds this range,  $\mu_i$  decreases. While the increased braking speed not only increases the maximum  $T_i$ , but also increases the increasing rate of  $T_i$ . This indicates that the increase of maximum  $T_i$  of brake pad mainly depends on the braking speed. As long as the braking speed is constant, the influence of braking time and braking pressure on maximum temperature is limited.

The  $\mu_i$  and  $T_i$  of AF and OF at low braking speed (160 km/h) and different pressures are shown in Fig. 6. The variation of  $\mu_i$  and  $T_i$  at 0.21 MPa is shown in Fig. 6(a) and (b). From Fig. 6(a),  $\mu_i$  of AF and OF has the similar fluctuation and value for the first 50 s. However, during the final stage of braking, the rise of  $\mu_i$  of AF is significantly higher than that of OF, which indicates that the friction surface of AF can provide greater friction resistance to the counterface. From Fig. 6(b), the  $T_i$  of OF is slightly higher than that of AF, but the difference of  $T_i$  between AF and OF is small. When the pressure is 0.41 MPa, from Fig. 6(c) and (d), the fluctuation of  $\mu_i$  and  $T_i$  of AF and OF is similar to that at 0.21 MPa, but the  $\mu_i$  is slightly lower, which is consistent with the description about the influence rules of pressure. As the pressure increases to 0.57 MPa,  $\mu_i$  of AF is obviously lower than that of OF during the whole braking process. This means that AF is more sensitive to the pressure when the pressure exceeds a certain value. Overall,  $\mu_i$  of AF and OF ranges from 0.35 to 0.6 at three different pressures. Except for the last few seconds of braking time, the range of  $\mu_i$  is the ideal range for a braking system (0.35–0.5) [7]. Through the studies of Ilo et al. [23] and So et al. [24], the  $\mu_i$  is at the range of 0.4–0.6 when the friction occurs between iron oxides and the  $\mu_i$  decreases with the addition of graphite [25]. Further, Rodrigues [7] also pointed out that pure  $\text{Fe}_3\text{O}_4$  between contact surface provides  $\mu_i$  in the range of 0.4–0.45 and the binary Cu-magnetite mixtures tested at room temperature promote higher  $\mu_i$  (0.47–0.71). From those we can roughly analyze the variation of composition of tribo-film on the friction surface at 160 km/h. At the beginning of the braking, although there is large friction resistance from copper and hard particles on the friction surface, the amount of graphite exposed to the surface is high, which induces the lower  $\mu_i$  (0.35). As the braking continuous, the graphite is covered by a gradually formed tribo-oxide film and the abrasive particles re-extruded on the friction surface, which promote the increase of  $\mu_i$ . In addition, some broken graphite is still present in the friction film, which leads to a lower  $\mu_i$  (0.35–0.6) than mentioned when using the binary Cu-magnetite mixtures (0.47–0.71) [7]. From Fig. 5(b),(d) and (f), the  $T_i$  of OF is slightly higher than that of AF at 0.21 MPa and 0.41 MPa, but the difference of  $T_i$  is not significant.

The  $\mu_i$  and  $T_i$  of AF and OF at high braking speed (350 km/h) and different pressures are shown in Fig. 7. Fig. 7(a) and (b) exhibit the variations of  $\mu_i$  and  $T_i$  under severe braking conditions (0.41 MPa, 350 km/h). In Fig. 7(a), during the braking period of 0–50 s,  $\mu_i$  of OF increases, and then decreases rapidly until the end of braking procedure. For AF,  $\mu_i$  also goes up in the braking time of 0–50 s, and then stays more stable in the braking time of 50–70 s than that of OF. The occurrence of platform stage is related to the stabilization of the material on the friction surface, which attributes to the contribution of fiber additive. In Fig. 7(b), the maximum  $T_i$  of AF is about 30 °C lower than that of OF, suggesting that AF has better applicability for braking at high speed than OF. As the pressure increases to 0.57 MPa, the variation of  $\mu_i$  and  $T_i$  shown in Fig. 7(c) and (d) is similar to that at

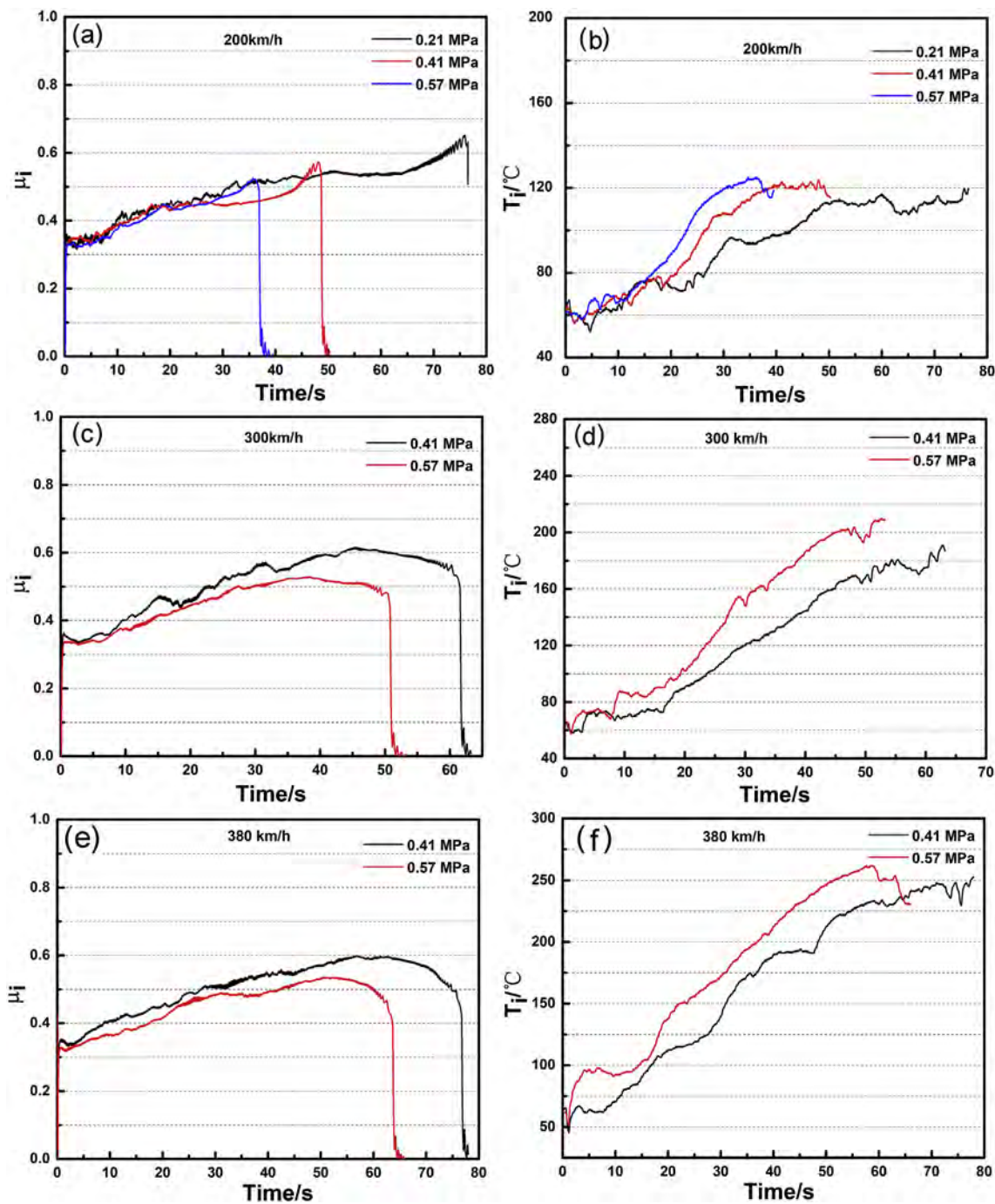


Fig. 4. Instantaneous friction coefficient ( $\mu_i$ ) and temperature ( $T_i$ ) of AF at different braking speeds and pressures during an emergency braking: (a, b) 200 km/h, 0.21 MPa–0.57 MPa; (c, d) 300 km/h, 0.41 MPa–0.57 MPa; (e, f) 380 km/h, 0.41 MPa–0.57 MPa.

0.41 MPa.

Fig. 8 shows the mean friction coefficient ( $\mu_m$ ) at different braking speeds and pressures, corresponding to the testing process shown in Fig. 2. At the first stage (I) (0.21 MPa, 120 km/h - 220 km/h), the  $\mu_m$  increases when the braking speed increases from 120 km/h to 200 km/h and then decreases once the braking speed reaches 220 km/h. Besides,  $\mu_m$  of AF is higher than that of OF. As the braking pressure increases to 0.41 MPa at the second stage (II),  $\mu_m$  of OF and AF increases gradually as the increase of braking speed. The contact plateaus formed by compaction of wear debris and tribo-oxide film start breaking down and then act as hard particles under the interfacial contact to hinder the rotation of the brake disc, which induces the increase of  $\mu_m$  [26,27]. Meanwhile,  $\mu_m$  of AF is also higher than that of OF when the braking

speed is less than 300 km/h. At the first stage (I) and second stage (II),  $\mu_m$  ranges from 0.35 to 0.55, while at third stage (III), the pressure increases to 0.57 MPa and the range of  $\mu_m$  is small (0.35–0.48) and the increasing rate of  $\mu_m$  is slow before 300 km/h. Once the braking speed exceeds 300 km/h,  $\mu_m$  maintains relative stable. After testing stages (I) - (III), the  $\mu_m$  of two samples in the fourth stage (IV) is obvious lower than that at the second stage (II) under the same braking conditions. This is due to flatter friction surface resulting from the repeated extrusion and deformation. Nevertheless, even after a series of emergency braking,  $\mu_m$  at the fourth stage (IV) is in the range of 0.35–0.36, which is suitable for the high-speed railway train [18]. Overall, AF shows slightly higher  $\mu_m$  at the first stage and the second stage, while  $\mu_m$  of two samples are similar at the third stage (III) and the fourth stage (IV).

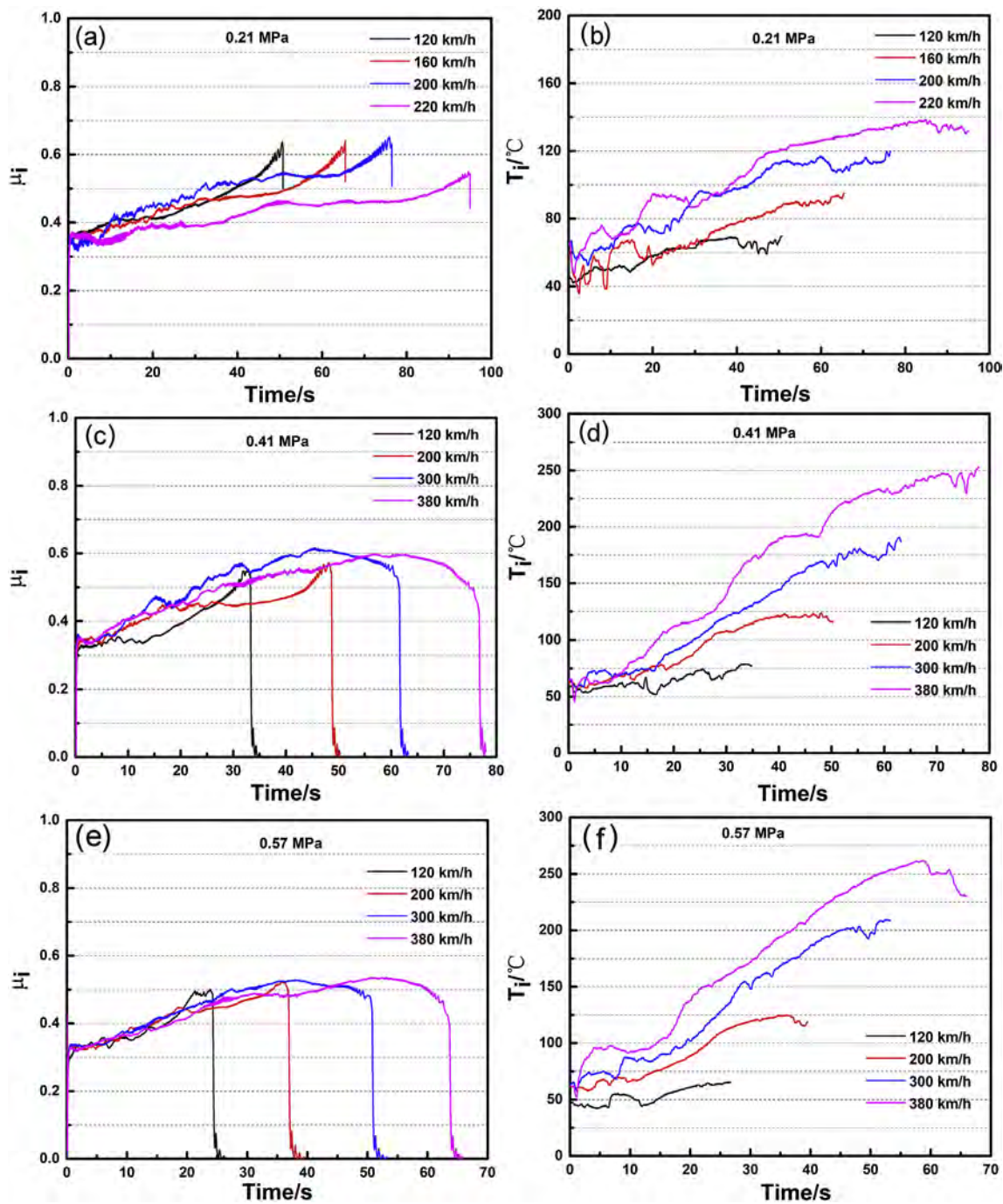


Fig. 5. Instantaneous friction coefficient ( $\mu_i$ ) and temperature ( $T_i$ ) of AF at different braking speed and pressures during an emergency braking: (a, b) 0.21 MPa, 120 km/h – 380 km/h; (c, d) 0.41 MPa, 120 km/h – 380 km/h; (e, f) 0.57 MPa, 120 km/h – 380 km/h.

This is attributed to the fact that  $Al_2O_3$  fiber can contribute to the surface roughness at lower pressure and braking speed and the flatter friction surface at higher braking speed and pressure can eliminate this effect from  $Al_2O_3$  fiber. Table 4 shows the wear loss of AF and OF at the end of testing. It is significant that the addition of  $Al_2O_3$  fiber additive can greatly reduce the wear loss. For AF, wear loss decreased by 45% compared with the sample without fiber additives.

Since the stability of  $\mu_m$  is significant for steady braking operation and low vibration, it is evaluated by a term of friction stability (FS) in Fig. 9 [15]:

$$FS = \frac{\mu_{mean}}{\mu_{max}} \quad (1)$$

where  $\mu_{mean}$  is the mean friction coefficient and  $\mu_{max}$  is the maximum friction coefficient. The higher FS means a stable braking performance in friction coefficient. At the first stage (I), as the braking speed increases, FS of AF increases from 0.7 to 0.78 while FS of OF is in the range of 0.72–0.8. At 220 km/h, FS of AF is suddenly higher than that of OF. As the braking pressure is increased at the second stage (II), OF shows the higher FS (0.8–0.9) when the braking speed is less than 300 km/h. AF shows the low FS, which initially decreases at first and then increases as the braking speed increases. When the braking speed exceeds 300 km/h, FS of OF decreases from 0.9 to 0.82 while AF maintain the stable FS (0.82–0.83). At the third stage (III) with the highest pressure (0.57 MPa), the fluctuation of FS is similar to that at the second stage (II): when the braking speed is less than 30 km/h, the

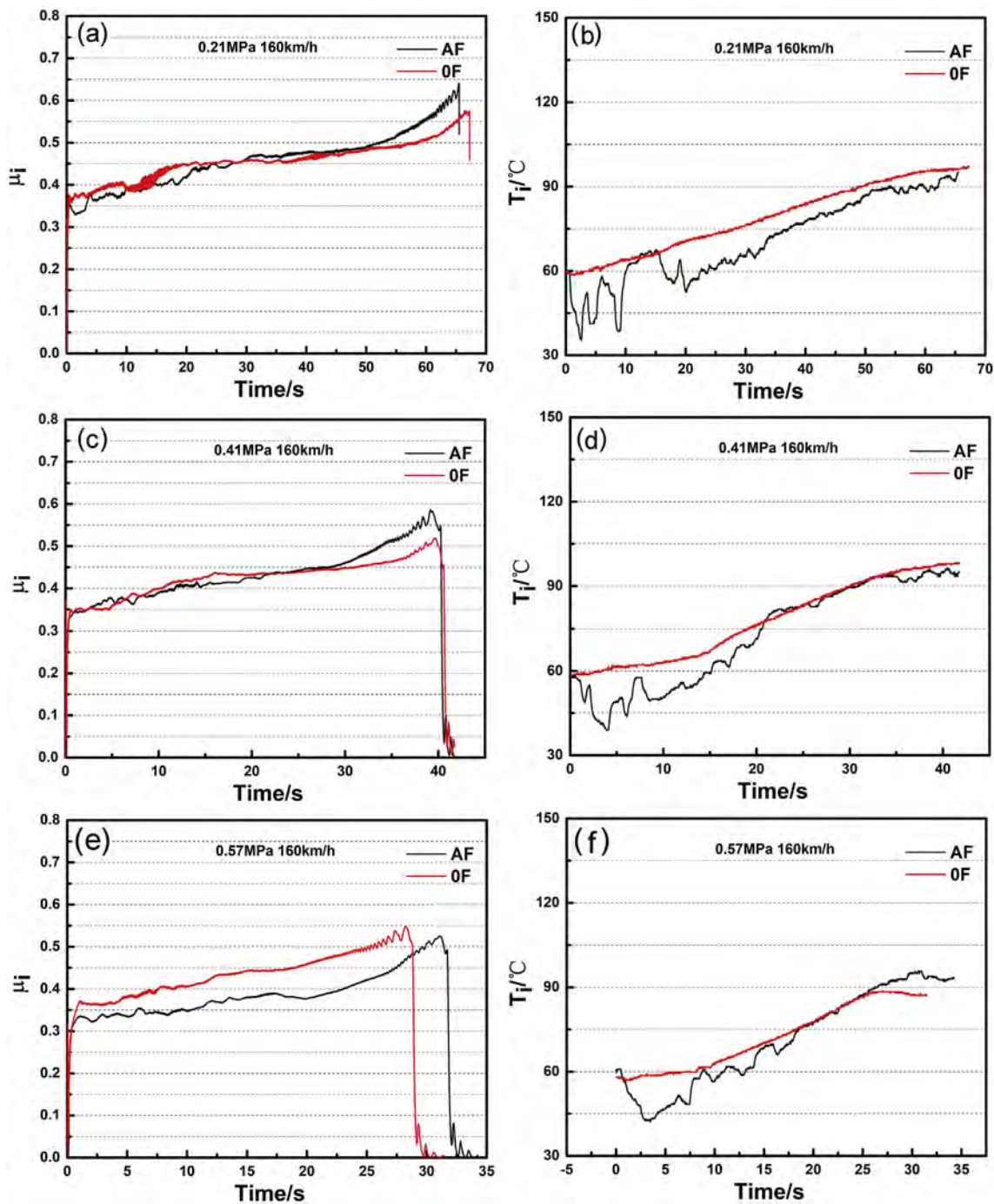


Fig. 6. Instantaneous friction coefficient ( $\mu_i$ ) and temperature ( $T_i$ ) of AF and OF at 160 km/h and different pressures during an emergency braking: (a, b) 0.21 MPa, 160 km/h; (c, d) 0.41 MPa, 160 km/h; (e, f) 0.57 MPa, 160 km/h.

stability rating of the composites is:  $OF > AF$ ; as the operating conditions of speed become more severe ( $> 300$  km/h), the FS of OF decreases rapidly, while FS of AF also maintains about 0.84. At the fourth stage (IV), FS of OF exhibits an obvious decline (from 0.86 to 0.68) and it is lower than that at the second stage (II) (0.8). However, for AF, FS at the fourth stage is similar to that at the second stage. Overall, when the braking speed is less than 300 km/h, the OF shows higher FS and once the braking speed exceeds 300 km/h, AF exhibits more stable  $\mu_m$  under the more severe operating conditions (overload and higher braking speed).

### 3.3. Worn surface

The worn surface morphology of AF and OF at the end of testing was investigated by backscattered electron image (BSE image), as shown in Fig. 10. Fig. 10(a) shows the worn surface of AF. The friction surface is mainly composed of graphite and discontinuous tribo-film. Fig. 10(b) exhibits the worn surface of OF, showing a smoother tribo-film and graphite still exist simultaneously on the friction surface. However, compared with AF, the area covered by the tribo-film is larger. The rapid transferring of material to the friction surface would reduce the friction stability, which is consistent with the variation of FS of OF at higher braking speed and overload in Fig. 9. Less graphite is exposed on

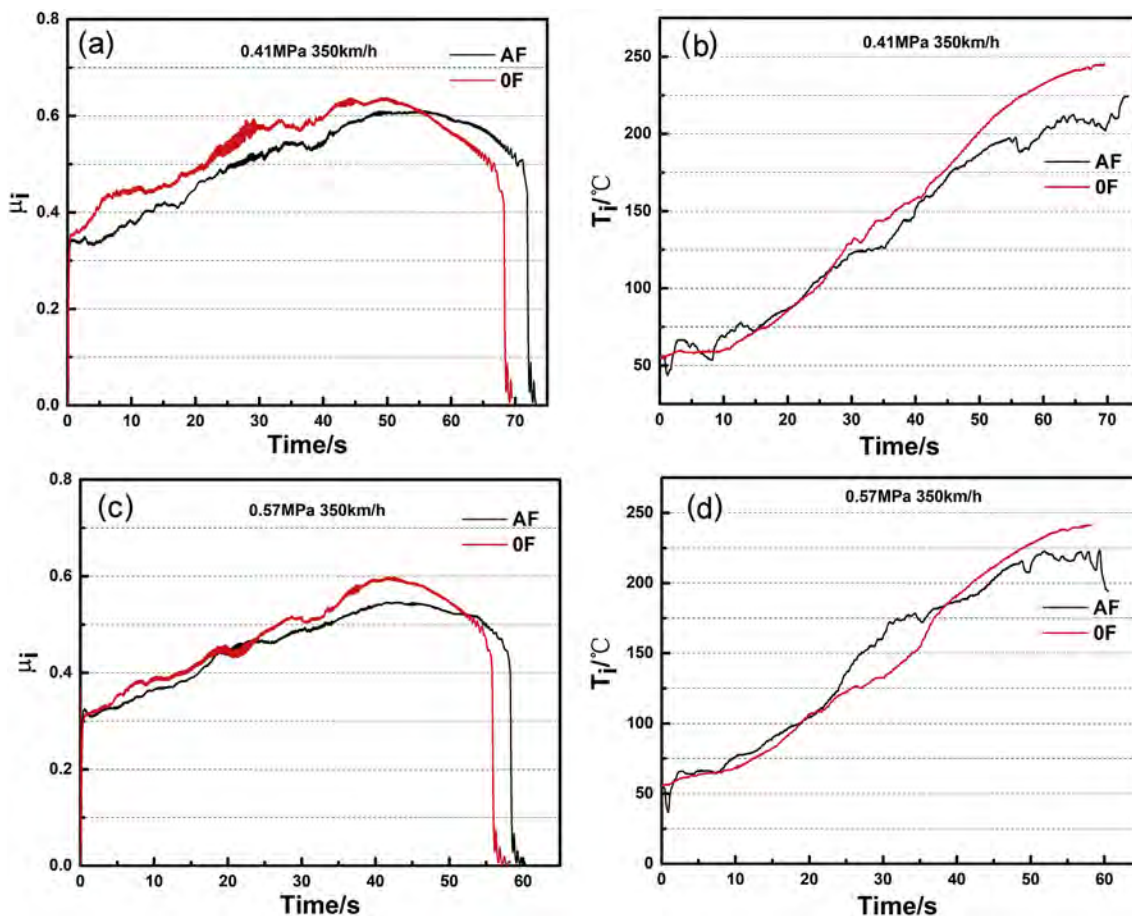


Fig. 7. Instantaneous friction coefficient ( $\mu_i$ ) and temperature ( $T_i$ ) of AF and OF at 350 km/h and different pressures during an emergency braking: (a, b) 0.41 MPa, 350 km/h and (c, d) 0.57 MPa, 350 km/h.

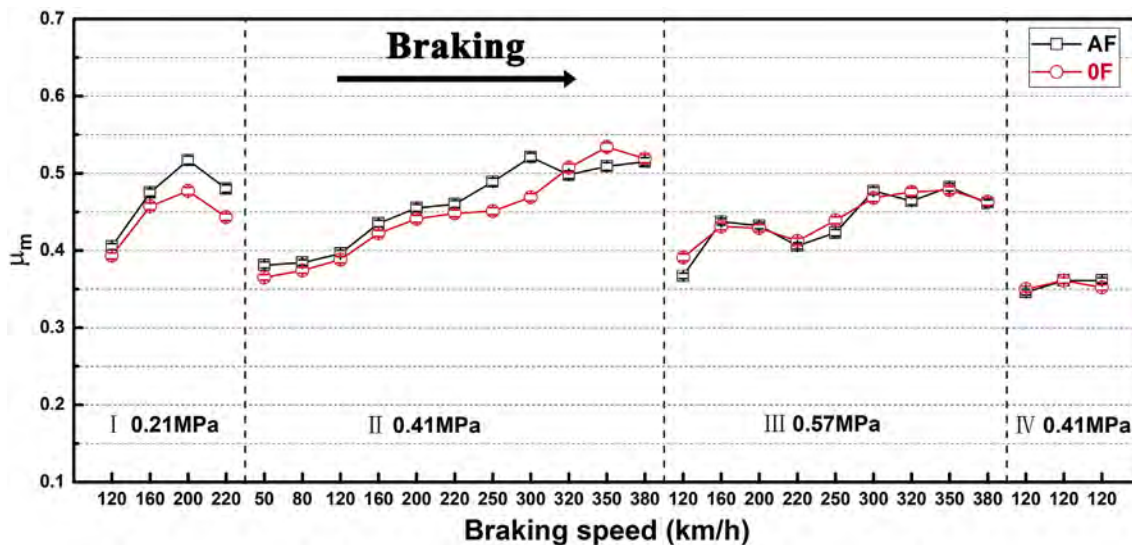


Fig. 8. Mean friction coefficient of AF and OF at different braking stages.

Table 4  
Wear loss of AF and OF.

Samples	AF	OF
Wear loss (g)	8.1 ± 0.03	14.9 ± 0.02

the friction surface which also contributes to the unstable friction coefficient and the higher maximum  $T_i$ . In order to observe the characteristic of the worn surface in detail, two different area on the worn surface of AF (A1 and A2) and OF (B1 and B2) are magnified in Fig. 10(c)–(f), respectively. From the magnified image of A1 in Fig. 10(c), although the friction surface of AF is not flat, the wear debris are fully compacted on the friction surface. No ploughing is observed on

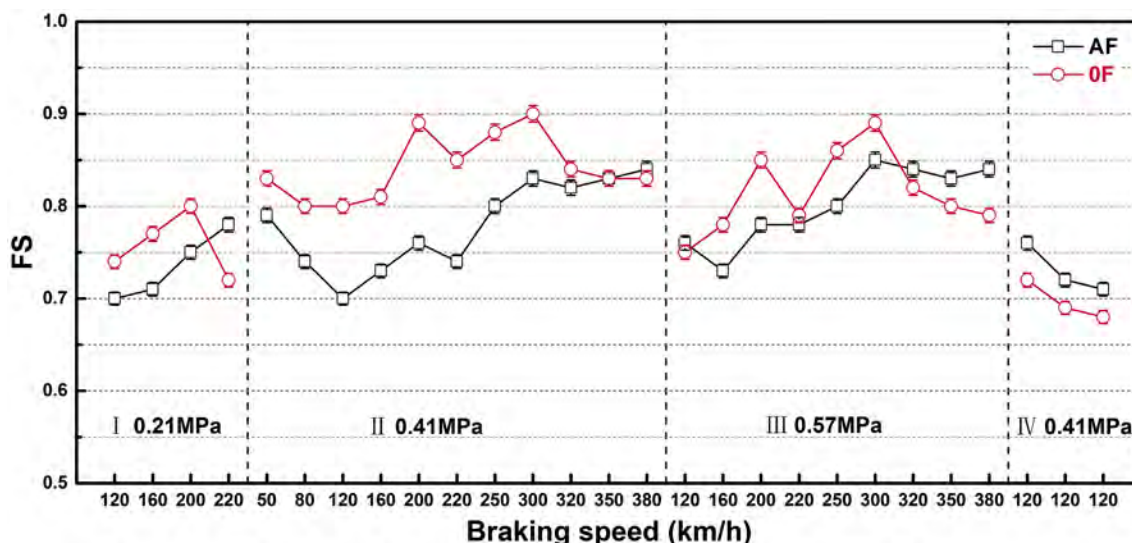


Fig. 9. Friction stability of AF and OF at different braking stages.

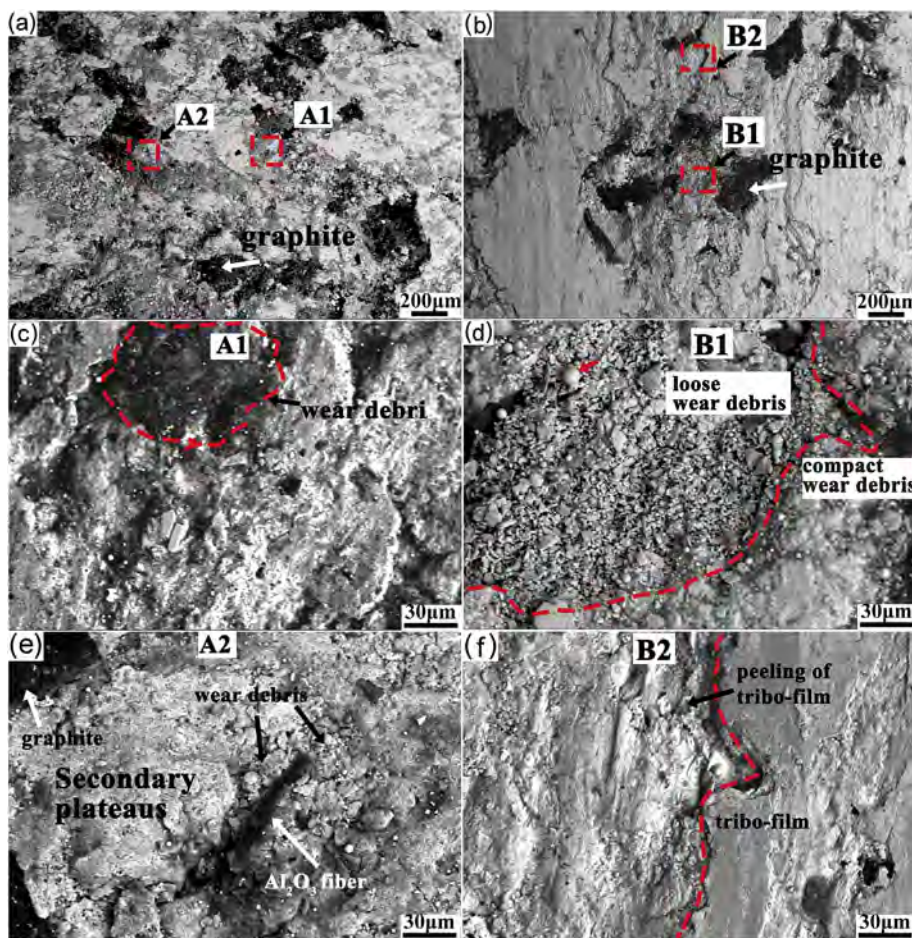


Fig. 10. BSE images of worn surface after the whole test: (a) AF; (b) OF; (c, e) corresponding magnified images of area A1 and A2 in (a), respectively; (d, f) corresponding magnified images of area B1 and B2 in (b), respectively.

the friction surface, indicating that abrasive wear is not the main wear mechanism. From the magnified image of B1 in Fig. 10(d), loose wear debris stores in the peeling pit. This also suggests the rapid transfer of material on the friction surface. The existence of spherical wear debris (red arrow) relates to the melting and solidification process, indicating the high flash temperature on friction surface. From the magnified

image of A2 in Fig. 10(e), Al<sub>2</sub>O<sub>3</sub> fibers are observed in the tribo-film and there is a lot of wear debris around the fibers. The Al<sub>2</sub>O<sub>3</sub> fiber acts as the primary plateaus and hinders the movement of wear debris, which reduce the wear loss. The magnified image of B2 in Fig. 10(f) exhibits the obvious existence of peeling of tribo-film. This results from the adhesion between the brake pad and counterface. Moreover, cyclic

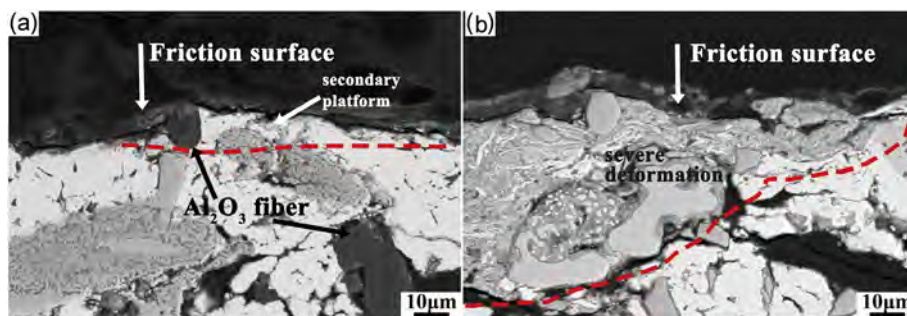


Fig. 11. Cross section of worn surface of AF and OF.

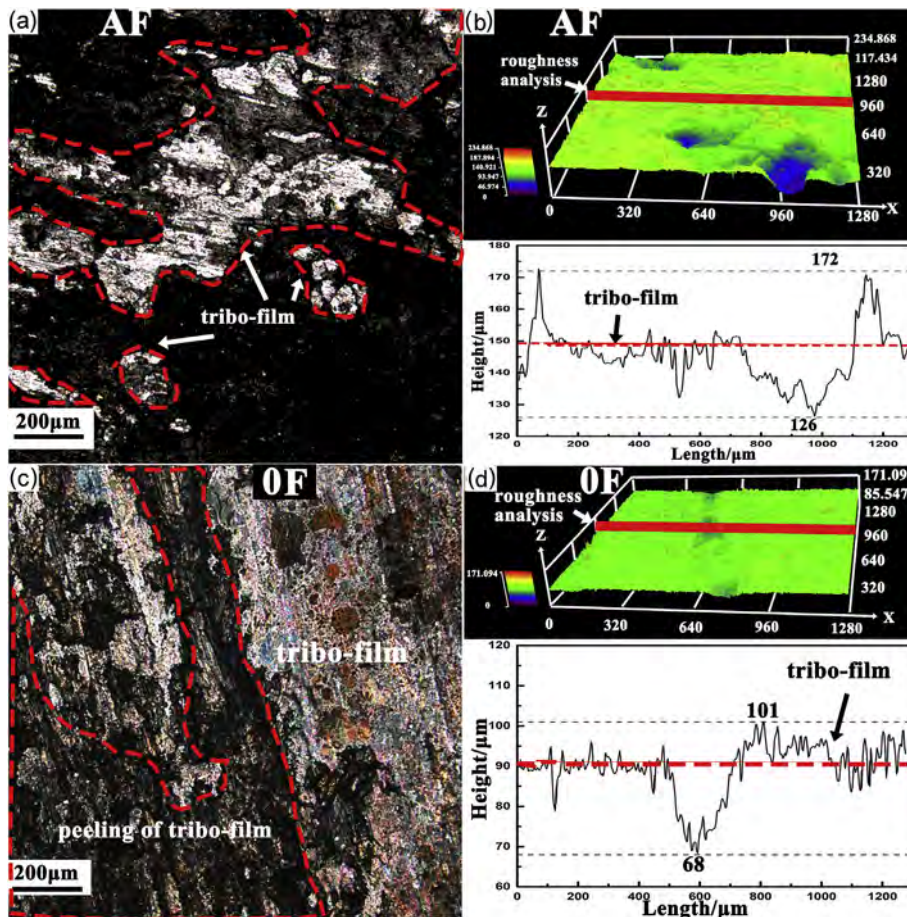


Fig. 12. Analysis of the worn surface covered by tribo-film and corresponding 3D morphology and roughness by laser scanning confocal microscope: (a, b) AF; (c, d) OF.

fatigue stress under high pressure can also accelerate peeling behavior. Peeling of large areas can increase wear loss and accelerate the flow of material.

Fig. 11 shows the cross section of worn surface of AF and OF. From Fig. 11(a), Al<sub>2</sub>O<sub>3</sub> fibers exist in both the friction surface and the substrate. The Al<sub>2</sub>O<sub>3</sub> fiber in the friction surface impedes the movement of softened surface material and promotes the formation of secondary plateaus, while Al<sub>2</sub>O<sub>3</sub> fiber in the substrate also bear the load and strengthen the substrate. From Fig. 11(b), the tribo-film on the friction surface is thicker and deformable severely.

For revealing the variation of surface height intuitively, a laser scanning confocal microscope was used to analyze the worn surface covered by the tribo-film, as shown in Fig. 12. In Fig. 12(a), the bright parts represent the discontinuous tribo-film covering the friction surface. In contrast with the black area, the tribo-film shows higher

heights. From the 3D morphology in Fig. 12(b), except for a few deep peeling pits, the difference in height between the bright and black areas is about 24 µm (from 150 µm to 126 µm). Some unusual high areas exist on the worn surface, and the height is about 22 µm (from 172 µm to 150 µm). Those areas are attributed to “elastic highlands”, which are expected to not contribute significantly to the friction force [28]. From Fig. 12(c), the bright regions are larger than that of AF. The peeling of the tribo-film is also shown in this Fig. 3D morphology in Fig. 12(d) shows a deep furrow with the depth of 22 µm (from 90 µm to 68 µm) on the worn surface. Compared with the roughness analysis in Fig. 12(b) and (d), the tribo-film of OF is smoother than that of AF.

Fig. 13 shows variation of surface height of the worn surface with no tribo-film. For AF in Fig. 13(a), there are many high platforms (marked by the red dash line). The size of the platforms is larger than 100 µm. From the corresponding 3D morphology in Fig. 13(b), the platforms are

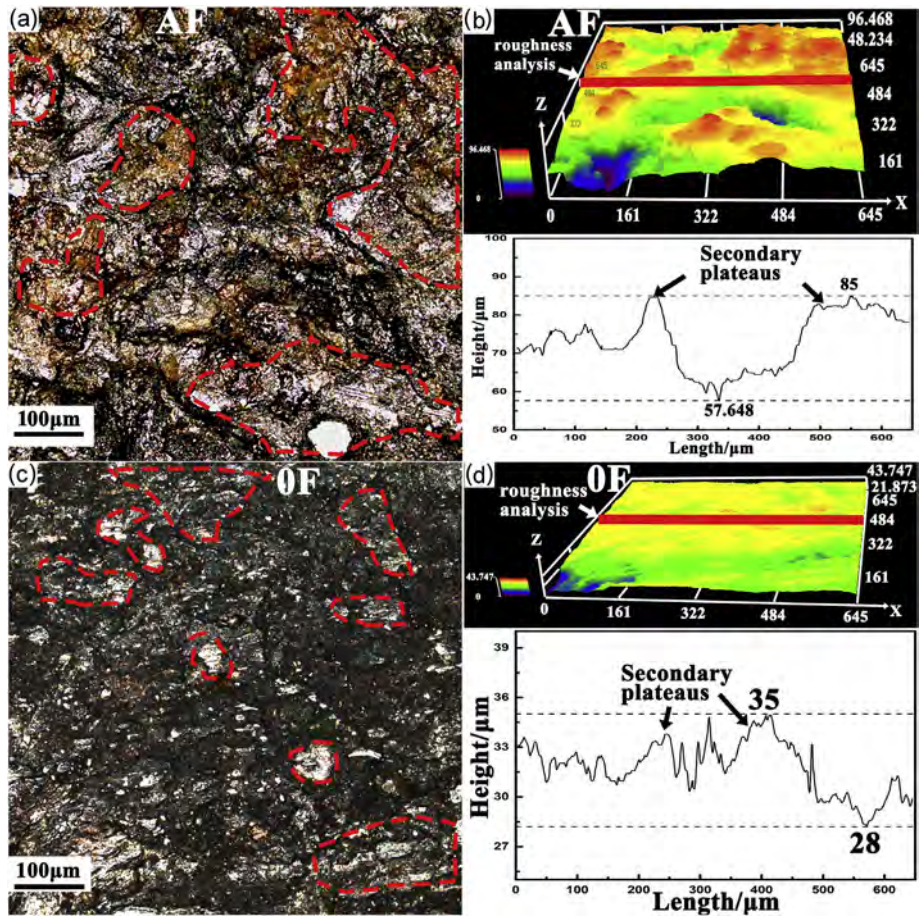


Fig. 13. Analysis of the worn surface with no tribo-film and corresponding 3D morphology and roughness by laser scanning confocal microscope: (a, b) AF; (c, d) OF.

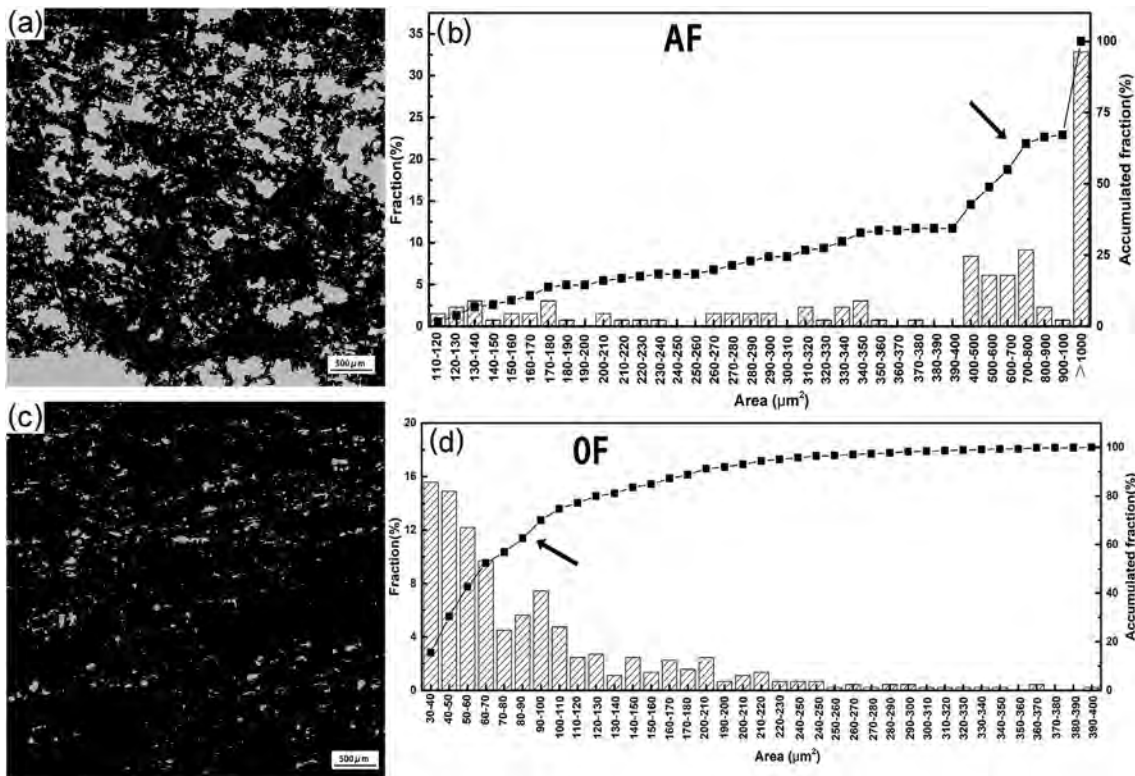


Fig. 14. Statistical analysis of the size distribution of the secondary plateaus on the worn surface: (a, b) AF; (c, d) OF.

pretty evident represented by the red regions. The height of the platform is about 27  $\mu\text{m}$  (from 85  $\mu\text{m}$  to 58  $\mu\text{m}$ ). For OF in Fig. 13(c), there are some less obvious platforms (marked by the red dash line) in the areas without tribo-film. Further, these platforms are much smaller in size than that shown in Fig. 13(a). From the 3D morphology in Fig. 13(d), a big yellow area covers this area. The difference of height of the platform is only about 7  $\mu\text{m}$  (from 35  $\mu\text{m}$  to 28  $\mu\text{m}$ ), which is far less than that in Fig. 13(b). It is this small difference in height that makes the insignificant color difference in the 3D morphological image.

In order to reveal the difference of secondary plateaus clearly, we analyzed the size distribution of the secondary plateaus on the worn surface of AF and OF, as shown in Fig. 14. By adjusting the contrast, the brighter regions of the image, which represents the higher surface area, are extracted using software, and the images of the processed examples are shown in Fig. 14(a) and (c). Fig. 14(b) and (d) are the statistical analysis of area distribution of the single bright region through five different region images similar to Fig. 14(a) and (c), respectively. For AF in Fig. 14(b), the size distribution of the secondary plateaus is low in the range of less than 400  $\mu\text{m}^2$ , and the accumulated fraction is only about 30%. Most of the size of the secondary plateaus distributes in the range more than 400  $\mu\text{m}^2$ , especially when the size exceeds 1000  $\mu\text{m}^2$ , and the percentage is up to 30%. However, for OF in Fig. 14(d), the size of secondary plateaus is mainly less than 200  $\mu\text{m}^2$ , and the accumulation fraction exceeds 90%. This indicates that the size of secondary plateaus of OF is much smaller than that of AF.

Summarizing the characteristics of the worn surface from Figs. 10–13, we can speculate on the role of  $\text{Al}_2\text{O}_3$  fiber in the friction process. For  $\text{Al}_2\text{O}_3$  fibers exposed to the friction surfaces, the movement of wear debris and softened material is impeded by  $\text{Al}_2\text{O}_3$  fiber, which promotes the formation of secondary plateaus and contributes to the stable friction coefficient at high braking speed and pressure. The slower flow of material and lower release of wear debris on the friction surface also greatly reduce the wear loss. In addition,  $\text{Al}_2\text{O}_3$  fiber acts as a friction component, inducing the high friction coefficient. The  $\text{Al}_2\text{O}_3$  fibers existing in the substrate can resist the deformation of the worn surface and prevent damage from the secondary plateaus. According to Noh and Jang [30], the correlation between static friction and total contact area was poor, and the static friction coefficient is high when there are high secondary plateaus on the worn surface. This can explain well that the AF shows the rapid increase of friction coefficient at the end of each braking. For the sample with no fiber (OF), the tribo-film is weak due to a lack of the strengthening phase. Under lower braking speed (< 300 km/h), the tribo-film is easier to form on the friction surface, inducing the high FS. When the braking speed exceeds 300 km/h, the weak tribo-film of OF peels off easily, which causes the higher wear loss. The material on the friction surface flows easily and form a thick tribo-film. Under cyclic shear stress, the weak tribo-film can deform violently, which is also the reason that OF shows the fade and fluctuated friction coefficient at high braking speed and pressure.

#### 4. Conclusions

Copper-based brake pads were fabricated by utilizing  $\text{Al}_2\text{O}_3$  fiber additives and tested from mild braking conditions to severe braking conditions. From the detailed investigation of the variation of friction coefficient, wear loss, temperature and tribo-film caused by the addition of  $\text{Al}_2\text{O}_3$  fiber, it is found that:

- (1) The new test procedures can distinguish the braking performance of different samples under different test conditions. For the same sample, the maximum temperature of brake pads mainly depends on the braking speed. Once the braking speed is constant, braking pressure shows only a slightly influence. However, the increasing rate of temperature can be accelerated by the increased braking speed and pressure. For the different samples, the sample with  $\text{Al}_2\text{O}_3$  fiber additive exhibits the lower maximum temperature

during braking than that with no fiber additives. Especially at higher braking speed, the decline of temperature is up to 30  $^\circ\text{C}$ , which is about 14% of maximum.

- (2) Compared to the sample with no fiber additive, at lower braking speed and pressure, the sample with  $\text{Al}_2\text{O}_3$  fiber exhibits higher  $\mu_m$ .  $\text{Al}_2\text{O}_3$  fiber acts as a friction component between the contact surface of the brake pad and disc and improves the surface roughness.
- (3) At higher braking speed and overload, the flatter friction surface can eliminate the effect of surface roughness from  $\text{Al}_2\text{O}_3$  fiber. However, the  $\text{Al}_2\text{O}_3$  fiber additives can still improve the stability of  $\mu_m$  effectively.  $\text{Al}_2\text{O}_3$  fiber exists in the tribo-film and acts as the primary plateaus, and then promotes the formation of high-strength secondary plateaus by hindering the rapid transferring of surface material. The  $\text{Al}_2\text{O}_3$  fibers existing in the substrate can also resist the deformation of the worn surface and prevent damage from the secondary plateaus. Those are also the reasons that wear loss of AF greatly decreased by 45% compared with the sample with no fiber additives.

#### Acknowledgements

This work is financially supported by National Key R&D Program of China (2016YFB0301400) and National Natural Science Foundation of China (51174029, 51574030).

#### References

- [1] SOHU, China. [https://www.sohu.com/a/255430031\\_99918722](https://www.sohu.com/a/255430031_99918722), [accessed 22 September 2018].
- [2] Xiong X, Chen J, Yao PP, Li SP, Huang BY. Friction and wear behaviors and mechanisms of Fe and  $\text{SiO}_2$  in Cu-based P/M friction materials. *Wear* 2007;262:1182–6.
- [3] Peng T, Yan QZ, Zhang XL. Stability of metal matrix composite pads during high-speed braking. *Tribol Lett* 2018;66:63.
- [4] Peng T, Yan QZ, Li G, Zhang XL. The influence of Cu/Fe ratio on the tribological behavior of brake friction materials. *Tribol Lett* 2018;66:18.
- [5] Kovalchenko AM, Fushchich OI, Danyluk S. The tribological properties and mechanism of wear of Cu-based sintered powder materials containing molybdenum disulfide and molybdenum diselenite under unlubricated sliding against copper. *Wear* 2012;290–291:106–23.
- [6] Xiao YL, Zhang ZY, Yao PP, Fan KY, Zhou HB, Gong TM. Mechanical and tribological behaviors of copper metal matrix composites for brake pads used in high-speed trains. *Tribol Int* 2018;119:585–92.
- [7] Rodrigues ACP, Österle W, Gradt T, Azevedo CRF. Impact of copper nanoparticles on tribofilm formation determined by pin-on-disc tests with powder supply: addition of artificial third body consisting of  $\text{Fe}_3\text{O}_4$ , Cu and graphite. *Tribol Int* 2017;110:103–12.
- [8] Su LL, Gao F, Han XM, Chen JG. Effect of copper powder third body on tribological property of copper-based friction materials. *Tribol Int* 2015;90:420–5.
- [9] Xiong X, Chen J, Yao PP, Li SP, Huang BY. Friction and wear behaviors and mechanisms of Fe and  $\text{SiO}_2$  in Cu-based P/M friction materials. *Wear* 2007;262:1182–6.
- [10] Baghani M, Aliofkhaezrai M, Askari M. Cu–Zn– $\text{Al}_2\text{O}_3$  nanocomposites: study of microstructure, corrosion, and wear properties. *Int J Min Met Mater* 2017;24:462–72.
- [11] Bijwe J. Composites as friction materials: recent developments in non-asbestos fiber reinforced friction materials—a review. *Polym Compos* 1997;18:378–96.
- [12] Dong F, Blum FD, Dharani LR. Lapinus fibre reinforced phenolic composites: flexural and friction properties. *Polym Compos* 1996;4:155–61.
- [13] Satapathy BK, Bijwe J. Fade and recovery behavior of non-asbestos organic (NAO) composite friction materials based on combinations of rock fibres and organic fibers. *J Reinf Plast Compos* 2005;24:563–77.
- [14] Singh T, Patnaik A. Performance assessment of lapinus-aramid based brake pad hybrid phenolic composites in friction braking. *Arch Civ Mech Eng* 2015;15:151–61.
- [15] Kolluri D, Ghosh AK, Bijwe J. Analysis of load-speed sensitivity of friction composites based on various synthetic graphites. *Wear* 2009;266:266–74.
- [16] Wang T, Shozaki M, Yamamoto M, Kagawa A. Synergy effect of reinforcement particle, fiber and matrix on wear resistance of hybrid metal matrix composite fabricated by low pressure infiltration process. *Mater Des* 2015;66:498–503.
- [17] Wang YQ, Afsar AM, Jang JH, Han KS, Song JI. Room temperature dry and lubricant wear behaviors of  $\text{Al}_2\text{O}_3/\text{SiCp}/\text{Al}$  hybrid metal matrix composites. *Wear* 2010;268:863–70.
- [18] TJ/CL 307-2014. Brakes-disc brakes and their application-provisional conditions for the approval of brake pads intended for high-speed EMUs. issued by China Railway Corp. 2014. [in Chinese].
- [19] Peng T, Yan QZ, Li G, Zhang XL, Wen ZF, Jin XS. The braking behaviors of Cu-based

- metallic brake pad for high-speed train under different initial braking speed. *Tribol Lett* 2017;65:135.
- [20] Lv M, Zheng F, Wang QH, Wang TM, Liang YM. Friction and wear behaviors of carbon and aramid fibers reinforced polyimide composites in simulated space environment. *Tribol Int* 2015;92:246–54.
- [21] Gultekin D, Uysal M, Aslan S, Alaf M, Guler MO, Akbulut H. The effects of applied load on the coefficient of friction in Cu-MMC brake pad/Al-SiCp MMC brake disc system. *Wear* 2010;270:73–82.
- [22] Uyyuru RK, Surappa MK, Brusethaug S. Tribological behavior of Al-Si-SiCp composites/automobile brake pad system under dry sliding conditions. *Tribol Int* 2007;40:365–73.
- [23] Ilo S, Tomala A, Badisch E. Oxidative wear kinetics in unlubricated steel sliding contact. *Tribol Int* 2011;44:1208–15.
- [24] So H, Yu DS, Chuang CY. Formation and wear mechanism of tribo-oxides and the regime of oxidational wear of steel. *Wear* 2002;253:1004–15.
- [25] Österle W, Dmitriev AI, Orts-Gil G, Schneider T, Ren H, Sun X. Verification of nanometre-scale modelling of tribofilm sliding behavior. *Tribol Int* 2013;62:155–62.
- [26] Satapathy BK, Bijwe J. Performance of friction materials based on variation in nature of organic fibres Part I: fade and recovery behavior. *Wear* 2004;257:573–84.
- [27] Dadkar N, Tomar BS, Satapathy BK, Patnaik A. Performance assessment of hybrid composite friction materials based on flyash-rock fiber combination. *Mater Des* 2010;31:723–31.
- [28] Neis PD, Ferreira NF, Fekete G, Matozo LT, Masotti D. Towards a better understanding of the structures existing on the surface of brake pads. *Tribol Int* 2017;105:135–47.
- [29] Aleman M, Gialanella S, Straffelini G, Ciudin R, Olofsson U, Perricone G, Metinoz I. Dry sliding of a low steel friction material against cast iron at different loads: characterization of the friction layer and wear debris. *Wear* 2017;376–377:1450–9.
- [30] Noh HJ, Jang H. Friction instability induced by iron and iron oxides on friction material surface. *Wear* 2018;400–401:93–9.
- [31] Qin FT, Gu JP, Zhang Y. Mechanism for friction reduction of ultrasonic vibration based on binomial theorem of tribology. *Micromotors* 2010;43:39–42.